

# On the Vertical Structure of Mesoscale Eddies in the Kuroshio-Oyashio Extension

H. Yao<sup>1</sup>, C. Ma<sup>1</sup>, and Z. Jing<sup>1,2</sup>

<sup>1</sup>Physical Oceanography Laboratory, Ocean University of China, Qingdao, China.

<sup>2</sup>Laoshan Laboratory, Qingdao, China.

Corresponding author: Chao Ma (machao@ouc.edu.cn)

## Key Points:

- Three vertical structures of mesoscale eddies are classified in the Kuroshio-Oyashio Extension region.
- Mesoscale eddy splitting or merging causes significant variation of vertical eddy structures.
- Different vertical eddy structures can be partially accounted for by differences in baroclinic instabilities.

## Abstract

Vertical structure of mesoscale eddies is key to the eddy-induced heat/material transport that further affects the climate and marine ecosystem. This study explores the vertical structure of mesoscale eddies in the Kuroshio-Oyashio Extension region (KOE) and its underlying dynamics. By applying the hierarchical ascending classification to the observational and reanalysis datasets, we classify mesoscale eddies with three distinct kinds of vertical structures. Each kind of eddies exhibits clear spatial aggregation along a distinct zonal band. Eddies have core depths of 100-300 m in the northern part of the KOE and core depths of 300-500 m and 0-100 m in the southern. The eddy splitting or merging does not introduce new kind of eddy vertical structure but causes large intra-kind variability. The different kinds of eddy vertical structures can be partially accounted for by the inference from the baroclinic instabilities at the eddy generation sites.

## Plain Language Summary

Mesoscale eddies are swirling motions with a radius ranging from several tens to a hundred of kilometers. The mesoscale eddies can cause strong vertical displacement of isopycnals, yet the vertical structure of such displacement has not been well understood. This study examines the vertical structures of mesoscale eddies in the Kuroshio-Oyashio Extension region based on the observational and reanalysis datasets. Mesoscale eddies with three distinct kinds of vertical structures are identified.

## 1 Introduction

Mesoscale eddies are ubiquitous in the upper ocean. Although the surface signals of mesoscale eddies have been well depicted based on satellite measurements, their vertical structures are less understood yet play a critical role in the eddy-induced heat/material transport. The latter has been shown to exert significant influences on the large-scale ocean thermal structure (Yu et al., 2019), anthropogenic climate changes (Du et al., 2022), ocean's biogeochemical cycles (McGillicuddy et al., 1998, 2007), dispersion of marine pollutants (Gilchrist et al., 2020) and microplastics behavior (Cai et al., 2022).

The Kuroshio-Oyashio Extension (KOE) region, located near the western boundary of North Pacific, consists of several prominent fronts including the subarctic front (SAF), the subarctic boundary (SAB), the Kuroshio bifurcation front (KBF) and the Kuroshio extension (KE) (Figure 1). The KOE region is characterized as a zone with elevated eddy kinetic energy (Qiu & Chen, 2010; Figure 1) and also a hotspot for mid-latitude air-sea heat and carbon dioxide exchanges (Fassbender et al., 2017; Jing et al., 2020). A knowledge of the vertical structure of mesoscale eddies within the KOE region is thus essential for understanding the eddies' climate and ecological impacts. By compositing all the mesoscale eddies around the KE front, Sun et al. (2017) reported that the eddy core measured by density anomaly is on average located around 300-400 m. In contrast, Dong et al. (2017) observed a deeper eddy core in the southern branch of the KE front than the northern branch and attributed this vertical difference to the poleward shoaling of thermocline. Ding and Jing (2020) analyzed the zonal variation of the eddy vertical structure, identifying double-core eddies in the upper stream of the KE front.

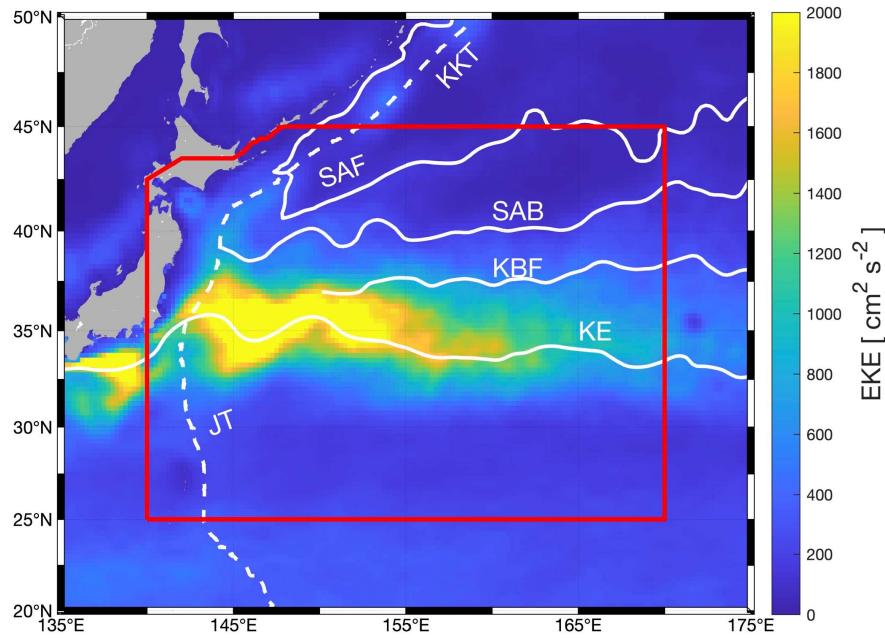


**Figure 1.** Climatological mean eddy kinetic energy (EKE; units:  $\text{cm}^2\text{s}^{-2}$ ) from AVISO (Aviso Altimetry, 2022). Japan Trench (JT) and Kuril-Kamchatka Trench (KKT) are represented by the dashed white lines. The Subarctic Front (SAF), the subarctic boundary (SAB), the Kuroshio Bifurcation Front (KBF) and the Kuroshio Extension (KE) are represented by white thick lines and are recognized by AVISO mean dynamic topography (MDT) contour following Nakano et al., (2018). The red box is our research region.

Although these previous studies have advanced the understanding of eddy vertical structures in the KOE region, they suffer from several limitations. First, the previous studies dealt with the mean eddy vertical structure in some pre-defined subdomains of the KOE region. It remains elusive from such analysis how many there are distinct kinds of eddy vertical structures in the KOE region. Second, the previous studies analyzed the eddy vertical structure under a Eulerian framework and thus did not take into account the evolution of eddy vertical structure during the eddy life cycle. In particular, it is still unclear whether the eddy vertical structure would change significantly during the eddy splitting or merging process. Third, mesoscale eddies in the KOE region are generated primarily from the baroclinic instability especially for those large enough to be well identified from the satellite altimeters (Ji et al., 2018; Yang et al., 2018). A natural question is that to what extent the distinct eddy vertical structures in the KOE region can be accounted for by the baroclinic instability.

Recently, clustering techniques have been leveraged to analyze oceanic data (Sambe & Suga, 2022). Surface-intensified and subsurface-intensified eddies have been distinguished via the hierarchical ascending classification (HAC) for the four primary eastern boundary upwelling systems (Pegliasco et al., 2015). In contrast to traditional approaches that manually subdivide areas for analysis, the HAC is capable of offering an impartial classification of mesoscale eddies based on the mathematical similarity of their vertical structures.

In this study, we explore the vertical structure of mesoscale eddies in the KOE region under a Lagrangian framework, by applying the HAC to the observational and reanalysis datasets. The paper is organized as follows. Section 2 details the data and methods. The vertical structures of

mesoscale eddies as well as their changes during the eddy splitting or merging are documented in Section 3. Section 4 discusses the role of baroclinic instability in shaping the eddy vertical structure. The paper is ended with a summary of its major conclusions.

## 2 Data and Methods

### 2.1 Observational Data

Surface mesoscale eddies within the KOE region (135-175°E; 25-45°N) are detected and tracked using daily maps of delayed-time multimission absolute dynamic topography (ADT) and derived geostrophic velocity fields (UV) (Pujol, 2022). The data span a period of 22 years (from January 2000 to December 2021) and have a spatial resolution of 1/4°. There are 3056 anticyclonic eddies (AEs) and 3787 cyclonic eddies (CEs) detected and tracked in total via the TOEddies algorithm (Laxenaire et al., 2019). Only mesoscale eddies possessing more than five Argo profile within the maximum eddy velocity boundary during their lifespan are retained for further analysis. After a quality control of the Argo data (see Supplementary Text S1), there are 6105 (3547) Argo profiles in 394 AEs and 297 CEs used for analysis.

### 2.2 Reanalysis Data

Given the limitations in the spatio-temporal coverage of observational data, we have also utilized the Four-Dimensional Variational Ocean Reanalysis for the Western North Pacific over 30 Years (FORA-WNP30) (Usui et al., 2017) to analyze the vertical structure of mesoscale eddies and their underlying dynamics. The FORA-WNP30 offers a spatial resolution of 1/10° for the majority of the research region, and 1/6° for the remainder. To align with the period during which the assimilated altimeter-derived SSH was recorded, we only use model output from January 1993 to December 2014. From the FORA-WNP30 data, we detected and tracked 5100 AEs and 6371 CEs in total.

### 2.3 The Ocean Eddy Detection and Tracking Algorithms (TOEddies)

The TOEddies algorithm (Laxenaire et al., 2018, 2019), developed from the widely used geometric algorithm (Chaigneau et al., 2008, 2009; Pegliasco et al., 2015), is used to detect and track mesoscale eddies. The TOEddies algorithm does not only provide information on eddy dynamical characteristics such as radius and velocity but also constructs a sophisticated eddy network. This network connects eddy trajectories associated with merging with other eddies or splitting into multiple eddies, enabling the tracking the origin of individual eddies.

Once an eddy is detected, eddy anomalies are calculated by subtracting a local climatological mean profile. For the observational data, local climatological mean profiles of potential temperature  $\theta$ , salinity  $S$  and potential density  $\sigma$  are derived from the World Ocean Atlas 2018 (WOA18) 1/4° objectively analyzed monthly climatology following Laxenaire et al. (2020). These fields are linearly interpolated to match the position and day of the year of each Argo float. For the reanalysis data, eddy anomalies are calculated by subtracting a large-scale background field. The large-scale background of some variable, including  $\theta$ ,  $S$ ,  $\sigma$  and horizontal velocity ( $u, v$ ) is first computed as its climatological mean seasonal cycle over a 22-year period. Then this climatological mean seasonal cycle is further smoothed horizontally using a  $41 \times 41$

grid boxcar filter and temporally using a 31-day running mean filter. The eddy kinetic energy (EKE) is computed as  $EKE = (u'^2 + v'^2)/2$ .

## 2.4 Cluster Analysis

To classify mesoscale eddies with different vertical structures, we implement the HAC technique following Pegliasco (2015) to eddies in the observational and reanalysis datasets. Due to the complexity of mesoscale eddies in the KOE region, the vertical profiles of  $\theta'/S'/\sigma'$  at the centroids of the eddies and the average EKE profile along the SSH contour with the maximum eddy velocity are considered for a substantial classification.

All the vertical profiles are first linearly interpolated onto a 10-m regular grid from the surface to 1000 m, as the eddy signal below 1000 m in our research region is very weak. Then the vertical profiles of an eddy along its trajectory at different snapshots are averaged to form a single vertical profile. To remove potential obscure clusters classified by the HAC, following Laxenaire (2020) we discard weak eddies that have a maximum value of any vertical profile of  $\theta'/S'/\sigma'$  less than  $0.1\text{ }^{\circ}\text{C}/\text{psu}/\text{kg m}^{-3}$ . This criterion is applied to both the eddies in the observational and reanalysis data to keep consistency, yielding 394 (297) AEs (CEs) in the observational data and 3130 (4001) AEs (CEs) in the reanalysis data. Note that the much smaller number of eddies in the observation is due to the sparsity of Argo profiles.

The HAC method first treats each eddy's vertical profiles of  $\theta'/S'/\sigma'$  (and also EKE for the reanalysis data) as a unique cluster, subsequently merging similar clusters to form a unified cluster that encompasses all the eddies' vertical profiles. The merging process involves the three stages: calculating Euclidean distances of the normalized (dimensionless) vertical profiles between eddies; grouping closest eddies into a dendrogram using Ward's aggregation method (Ward, 1963); and finally selecting an optimal cut point in the cluster tree to best partition the eddies and retain significant clusters. Readers can refer to Pegliasco (2015) for more details of the HAC method.

## 3 Results

### 3.1 Vertical Structures of Mesoscale Eddies

Application of the HAC method to the observational data suggests that the vertical structures of AEs and CEs in the KOE region can be classified into three distinct clusters (Figure 2). The first cluster, including 112 (28%) AEs and 117 (39%) CEs, is characterized by strong  $\theta'/S'/\sigma'$  between 100 m and 300 m (Figure 2a, 2g, 2m, 2s, 2d, 2j, 2p and 2v). These eddies are predominantly located in the northern part ( $35^{\circ}\text{N}$ - $45^{\circ}\text{N}$ ) of the KOE region. Tracking analysis reveals that many AEs and CEs in this cluster originate from the Subarctic Front (SAF), the Kuril-Kamchatka Trench (KKT) and downstream KE (Supplementary Figures S1 and S2). The AEs (CEs) included in this cluster tend to carry positive (negative)  $\theta'$  and  $S'$  values with the former dominating  $\sigma'$ . The typical peaking values  $\theta'/S'/\sigma'$  in the vertical are  $1.97\text{ }^{\circ}\text{C}$ ,  $0.17\text{ psu}$ , and  $-0.20\text{ kg m}^{-3}$  for AEs and  $-1.91\text{ }^{\circ}\text{C}$ ,  $-0.22\text{ psu}$ , and  $0.15\text{ kg m}^{-3}$  for CEs, respectively. The water mass analysis implies that these eddies should carry Okhotsk Sea Mode Water (OSMW) (Yasuda, 1997; Gladyshev et al., 2003) and Transition Region Mode Water (TRMW) (Saito et al.,

2007), which is consistent with their origins derived from the tracking analysis (Supplementary Figure S3).

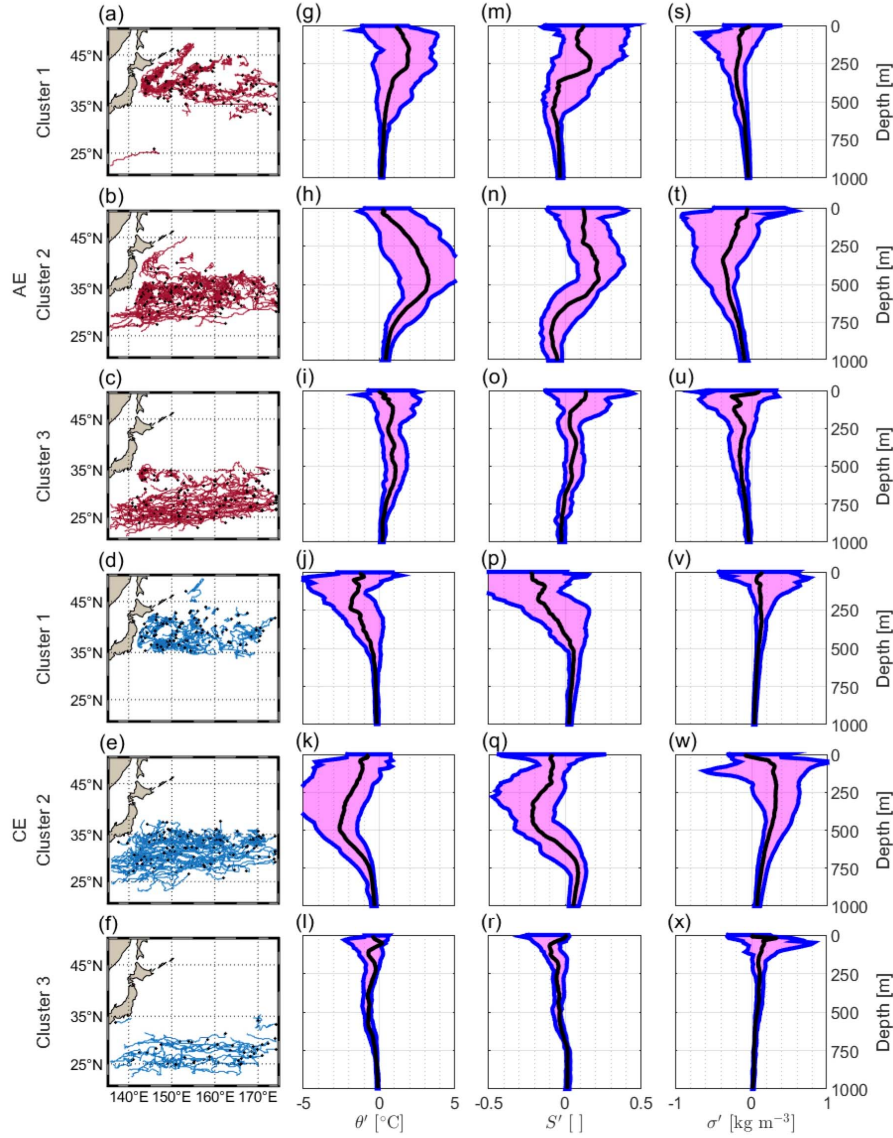


**Figure 2.** Spatial distributions and vertical structures ( $\theta'/S'/\sigma'$ ) of eddies for each cluster in the observational data. (a-f) The trajectories of eddies (red/blue line indicate AEs/CEs, the black diamond markers show the birth location), vertical profiles of (g-l) potential temperature, (m-r) salinity and (s-x) potential density anomaly for each eddy clusters. The black curve in each functional boxplot (Genton & Sun, 2020; Sun & Genton, 2011) is the median profile and the magenta box is the 50% central region.

The second cluster includes 164 (42%) AEs and 138 (46%) CE, exhibiting strong  $\theta'/S'/\sigma'$  between 300 m and 500 m (Figure 2b, 2h, 2n, 2t, 2e, 2k, 2q and 2w). This cluster is distributed around the center and to the south of the KE axis, located within the warm and salty region of the North Pacific Subtropical Mode Water (STMW) (Masuzawa, 1969) and Lighter Central Mode Water (L-CMW) (Oka et al., 2011) (Supplementary Figure S3). Some eddies in this cluster are shed off via the meandering of the KE (Ding & Jing, 2020), while others originate to the south of the KE axis or from the central North Pacific (Supplementary Figures S1 and S2). This

cluster displays typical peaking values of  $\theta'/S'/\sigma'$  as 3.25 °C, 0.22 psu, and -0.38 kg m<sup>-3</sup> for AEs and -2.62 °C, -0.22 psu, and 0.33 kg m<sup>-3</sup> for CEs.

The third cluster comprises 118 (30%) AEs and 42 (14%) CEs. The  $\theta'/S'/\sigma'$  of these eddies are near-surface intensified and have relatively smaller amplitudes than those in the first and second clusters (Figure 2c, 2i, 2o, 2u, 2f, 2l, 2r and 2x). Typical peaking values of  $\theta'/S'/\sigma'$  in this cluster are 1.08 °C, 0.14 psu, and -0.26 kg m<sup>-3</sup> for AEs, and -0.75 °C, -0.10 psu, and 0.33 kg m<sup>-3</sup> for CEs. This cluster of eddies is located in the southernmost part of the KOE region and partially overlapped with the second cluster of eddies in space. These eddies tend to form locally or originate from the central North Pacific, carrying warm and salty STMW (Supplementary Figures S1 to S3). To the best of our knowledge, this third eddy cluster has not been documented in the existing literature. Due to the spatial overlap of the second and third clusters, and the weaker amplitude of the third cluster, it is difficult to identify the third cluster based on the eddy composite analysis over a pre-defined region as done in the previous studies (Dong et al., 2017; Ji et al., 2018; Sun et al., 2017).

Finally, it is found that the three distinct eddy clusters in the observations are consistently reproduced in the reanalysis data (Supplementary Figure S4). The statistical analysis of surface characteristics within each cluster reveals notable distinctions among them (Supplementary Table S1 and S2). Moreover, whether including the vertical profile of EKE in the HAC method does not qualitatively affect the identified eddy clusters in the reanalysis data (Supplementary Figure S5). In the following analysis, we will focus on the eddy clusters in the reanalysis data as its sample number of eddies is much larger than that in the observation, yielding a more robust statistic.

### 3.2 Influences of eddy merging and splitting on vertical structures of mesoscale eddies

In the KOE region, displacement and deformation of mesoscale eddies cause frequent eddy merging and splitting. Among the total 5100 (6371) AEs (CEs) detected in the reanalysis data, only 2226 (2326) always evolve as a single coherent vortex. The remainings merge with other eddies or split into multiple eddies sometime during their life cycles. In specific, there are 1624 (2168) AEs (CEs) undergoing merging events and 1250 (1877) undergoing splitting events.

To examine the effects of eddy merging and splitting on the eddy vertical structures, we compute the vertical displacement of peaking depth of  $\sigma'$  during the merging and splitting events (denoted as  $d_m$  and  $d_s$ ). Here the vertical displacement is estimated as the difference between the peaking depths of  $\sigma'$  15 days before and after merging and splitting events. Sensitivity tests suggest that varying the time span from 10 to 20 days or using the peaking depth of  $\theta'$  and  $S'$  do not have substantial impacts on the results. It should be noted that the peaking depth of  $\sigma'$  during a 30-day-long period is likely to change even without the occurrence of eddy merging and splitting events. Therefore, the values of  $d_m$  and  $d_s$  should be compared to that when eddy merging and splitting do not occur (denoted as  $d_0$ ).

Figure 3 presents the probability density functions (PDFs) of  $d_m$ ,  $d_s$  and  $d_0$ . The mean value and standard deviation of  $d_0$  are 5.5±0.7 (6.6±0.9) m and 115.9±0.5 (143.7±0.6) m for AEs (CEs), respectively (the errorbars denote the 95% confidence intervals, and hereinafter). The standard deviation of  $d_m$  for AEs (CEs) increases to 215.5±5.4 (240.4±5.2) m, significantly larger than that of  $d_0$ . Similar is the case for  $d_s$ , suggesting that the eddy merging and splitting

have notable effects on the eddy vertical structures. Unlike the standard deviation, the difference among mean values of  $d_m$ ,  $d_s$  and  $d_0$  are minor. It thus suggests that the eddy merging and splitting should be unlikely to introduce new clusters of eddy vertical structures but instead enlarge the intra-cluster variability. This is further confirmed by applying the HAC method only to mesoscale eddies without merging or splitting events. The three re-classified clusters of eddy vertical structures are qualitatively consistent with those derived from all the eddies (Supplementary Figure S6).

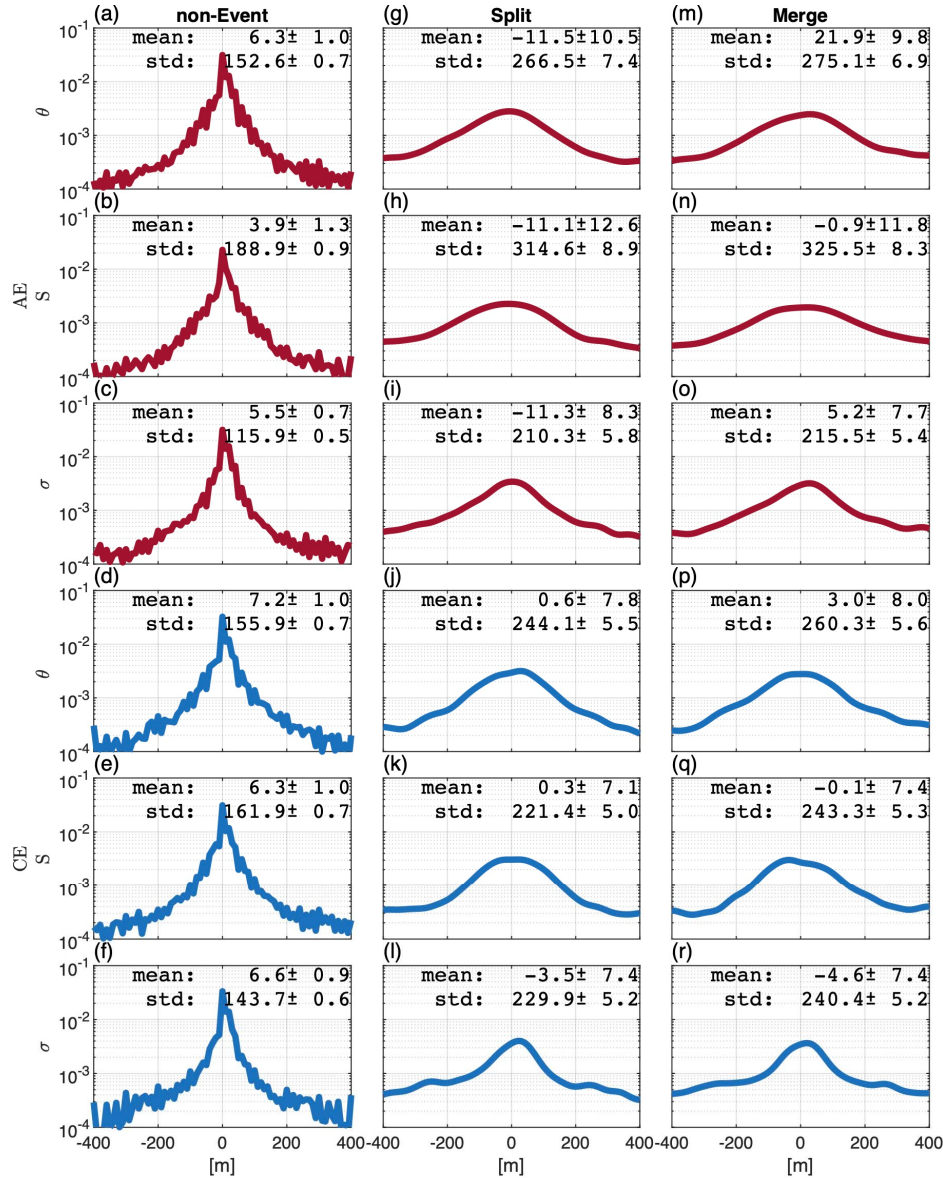


**Figure 3.** Probability density function of vertical displacement of peaking depth of  $\sigma'$  during the eddy merging, splitting events and otherwise (non-event). The errorbar denotes the 95% confidence intervals of the mean and standard deviation of vertical displacement.

## 4 Discussion

To shed light on the underlying dynamics on the three different clusters of vertical structures of mesoscale eddies in the KOE region, we perform a linear baroclinic instability (LBI)

analysis based on the inviscid quasi-geostrophic potential vorticity (QGPV) equation (Feng et al., 2022).

$$q_t' + \mathbf{U} \cdot \nabla q' + \mathbf{u}' \cdot \nabla Q = 0, \quad -H < z < 0 \quad (1.)$$

$$\varphi'_{zt} + U \cdot \nabla \varphi'_z + u' \cdot \nabla (\varphi'_z + f^{-1} N^2 \eta) = 0, \quad z = 0, -H, \quad (2.)$$

where  $\mathbf{U} = U(z)\vec{i} + V(z)\vec{j}$  is the mean current,  $Q = \beta y + \vec{k} \cdot \nabla \times \mathbf{U} - g/\rho_0 \partial_z (f\rho/N^2)$  is the mean potential vorticity with  $\beta$  the local planetary vorticity gradient,  $N^2$  the background squared buoyancy frequency,  $\rho_0$  the reference density and  $f$  the Coriolis parameter,  $q' = \nabla^2 \varphi' + \Gamma \varphi'$  is the eddy component of the QGPV with  $\Gamma = \partial_z (f^2/N^2 \partial_z)$  the vortex stretching operator,  $\mathbf{u}' = -\varphi'_y \vec{i} + \varphi'_x \vec{j}$  is the eddy velocity field expressed in terms of the horizontal eddy streamfunction  $\varphi' = \varphi'(x, y, z, t)$ ,  $\varphi'_z = V_z \vec{i} - U_z \vec{j}$  is proportional to the mean horizontal buoyancy gradient via the thermal wind relation,  $\eta$  is the bottom topography height at  $z = -H$  and  $\eta = 0$  at  $z = 0$ , and  $\nabla$  is the horizontal gradient operator.

Contrary to the previous LBI analysis adopting an Eulerian perspective (e.g., Jing et al., 2019), we employ a Lagrangian approach. In specific, the LBI analysis is computed based on the background field at the generation sites of individual eddies. To exclude the mixed-layer baroclinic instability (MLI) generating eddy at submesoscales, the upper boundary is moved from the sea surface to the 50-m depth. The detailed procedures for searching fastest-growing baroclinic instability (BCI) mode at mesoscales can be found in Feng et al. (2021 and 2022).

There are, however, several limitations for the LBI analysis. First, it can only account for mesoscale eddies generated primarily via the baroclinic instabilities. Second, it does not take into consideration the variation of eddy vertical structure during the evolution of mesoscale eddies especially the merging and splitting events. Given these limitations, it is unlikely that the variability of eddy vertical structures in the KOE region can be quantitatively reproduced from the LBI analysis. Instead, we attempt to explore whether the three distinct clusters of eddy vertical structures are qualitatively consistent with the inference from the LBI analysis.

Figure 4d shows the vertical profiles of  $|\varphi'|^2$  associated with mesoscale eddies belonging to different clusters. These vertical profiles can be compared to those of EKE. Although  $|\varphi'|^2$  for all the three clusters are surface-intensified, they decay with depth at different rates. The  $|\varphi'|^2$  of the first and second clusters has similar e-folding depths (174 m and 217 m), much larger than that (93 m) of the third cluster. This is qualitatively consistent with the decaying rates of EKE for these three clusters (Figure 4a-c). However, we note that although the vertical profiles of  $\theta'/S'/\sigma'$  of the first and second clusters are distinct from each other (Figure 2), their vertical profiles of EKE are almost the same. It thus implies that the different vertical eddy structures in the KOE region can only be partially accounted for by the baroclinic instability.

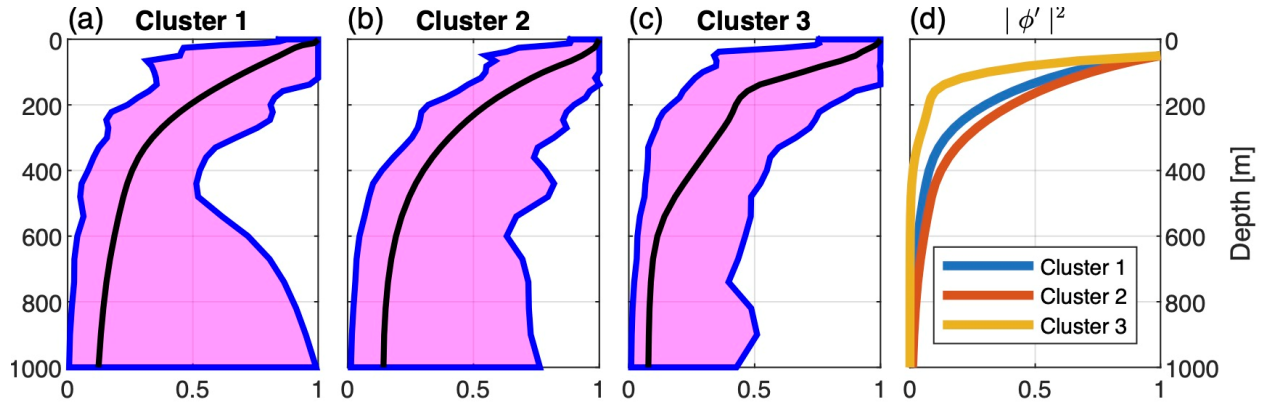


**Figure 4.** (a-c) Vertical profiles of normalized EKE for the three clusters in the KOE region. The black curve in functional boxplot (Genton & Sun, 2020; Sun & Genton, 2011) is the median vertical profile and the magenta box is the 50% central region. (d) Normalized median vertical profiles of  $|\phi'|^2$  derived from the LBI analysis computed at the generation sites of eddies belonging to the three clusters.

## 5 Conclusions

In this study, we utilize a clustering technique to classify the typical vertical structures of mesoscale eddies in the KOE region based on the observational and reanalysis data. According to the vertical profiles of  $\theta'/S'/\sigma'$ , three distinct eddy clusters are identified. The first cluster has core depths of 100-300 m and is located in the northern part of the KOE. The second and third clusters have core depths of 300-500 m and 0-100 m, respectively. These two clusters are located in the southern part of the KOE and overlapped in space. The eddy splitting or merging causes strong variability of vertical structures of  $\theta'/S'/\sigma'$ , enlarging their intra-cluster variability.

The LBI analysis at the eddy generation sites suggest that the three clusters of eddy vertical structures can only be partially accounted for by the inference from the baroclinic instabilities. Further research is needed to better comprehend the underlying dynamics governing the eddy vertical structures, including the effects of barotropic instability, eddy-mean flow, and eddy-eddy interactions.

## Acknowledgments

This research was supported by the National Natural Science Foundation of China (No.41676004). We thank Dr. Laxenaire for providing the TOEddies algorithm code and application testing.

## Data Availability Statement

The altimeter products were produced and distributed by CMEMS (Copernicus Marine and Environment Monitoring Service; [https://data.marine.copernicus.eu/product/SEALEVEL\\_GLO\\_PHY\\_L4\\_MY\\_008\\_047](https://data.marine.copernicus.eu/product/SEALEVEL_GLO_PHY_L4_MY_008_047)). The Argo data used here were provided by the Coriolis Global Data Acquisition Center (GDAC) of France ([ftp://ftp.ifremer.fr/ifremer/argo/geo/pacific\\_ocean/](ftp://ftp.ifremer.fr/ifremer/argo/geo/pacific_ocean/)). The climatological data WOA18 (World Ocean Atlas 2018) is produced and distributed by NOAA/NCEI (National Centers for Environmental Information; <https://www.ncei.noaa.gov/products/world-ocean-atlas>). The reanalysis data FORA-WNP30 (Four-dimensional Variational Ocean ReAnalysis for the Western North Pacific) produced by JAMSTEC (Japan Agency for Marine-Earth Science and Technology), and JMA/MRI (Meteorological Research Institute, Japan Meteorological

293 Agency) can be downloaded at <https://www.godac.jamstec.go.jp/fora/e/>. The radius of deformation data is calculated  
294 and published by Chelton ([https://ceoas.oregonstate.edu/rossby\\_radius](https://ceoas.oregonstate.edu/rossby_radius)). The seasonal mean data were processed by  
295 SSALTO/DUACS and distributed by AVISO+ (<https://www.aviso.altimetry.fr>) with support from CNES.  
296

297 **References**

- 298 Aviso Altimetry. (2022). *SSALTO/DUACS User Handbook: Climatologies products* [dataset].  
 299 [https://www.aviso.altimetry.fr/fileadmin/documents/data/tools/climatologies\\_hdbk.pdf](https://www.aviso.altimetry.fr/fileadmin/documents/data/tools/climatologies_hdbk.pdf)
- 300 Cai, M., Liu, M., Qi, H., Cui, Y., Zhang, M., Huang, P., Wang, L., Xie, M., Li, Y., Wang, W., Ke, H., & Liu, F.  
 301 (2022). Transport of microplastics in the South China Sea: A review. *Gondwana Research*, 108, 49–59.  
 302 <https://doi.org/10.1016/j.gr.2021.12.003>
- 303 Chaigneau, A., Eldin, G., & Dewitte, B. (2009). Eddy activity in the four major upwelling systems from satellite  
 304 altimetry (1992–2007). *Progress in Oceanography*, 83(1–4), 117–123.  
 305 <https://doi.org/10.1016/j.pocean.2009.07.012>
- 306 Chaigneau, A., Gizolme, A., & Grados, C. (2008). Mesoscale eddies off Peru in altimeter records: Identification  
 307 algorithms and eddy spatio-temporal patterns. *Progress in Oceanography*, 79(2–4), 106–119.  
 308 <https://doi.org/10.1016/j.pocean.2008.10.013>
- 309 Ding, Y., & Jing, C. (2020). Three-dimensional thermohaline anomaly structures of rings in the Kuroshio Extension  
 310 region. *Acta Oceanologica Sinica*, 39(3), 25–35. <https://doi.org/10.1007/s13131-020-1559-3>
- 311 Dong, D., Brandt, P., Chang, P., Schütte, F., Yang, X., Yan, J., & Zeng, J. (2017). Mesoscale Eddies in the  
 312 Northwestern Pacific Ocean: Three-Dimensional Eddy Structures and Heat/Salt Transports. *Journal of*  
 313 *Geophysical Research: Oceans*, 122(12), 9795–9813. <https://doi.org/10.1002/2017JC013303>
- 314 Du, T., Jing, Z., Wu, L., Wang, H., Chen, Z., Ma, X., Gan, B., & Yang, H. (2022). Growth of ocean thermal energy  
 315 conversion resources under greenhouse warming regulated by oceanic eddies. *Nature Communications*, 13(1),  
 316 7249. <https://doi.org/10.1038/s41467-022-34835-z>
- 317 Fassbender, A. J., Sabine, C. L., Cronin, M. F., & Sutton, A. J. (2017). Mixed-layer carbon cycling at the Kuroshio  
 318 Extension Observatory. *Global Biogeochemical Cycles*, 31(2), 272–288.  
 319 <https://doi.org/10.1002/2016GB005547>
- 320 Feng, L., Liu, C., Köhl, A., Stammer, D., & Wang, F. (2021). Four Types of Baroclinic Instability Waves in the  
 321 Global Oceans and the Implications for the Vertical Structure of Mesoscale Eddies. *Journal of Geophysical*  
 322 *Research: Oceans*, 126(3). <https://doi.org/10.1029/2020JC016966>
- 323 Feng, L., Liu, C., Köhl, A., & Wang, F. (2022). Seasonality of Four Types of Baroclinic Instability in the Global  
 324 Oceans. *Journal of Geophysical Research: Oceans*, 127(5). <https://doi.org/10.1029/2022JC018572>
- 325 Genton, M. G., & Sun, Y. (2020). Functional Data Visualization. In N. Balakrishnan, T. Colton, B. Everitt, W.  
 326 Piegorisch, F. Ruggeri, & J. L. Teugels (Eds.), *Wiley StatsRef: Statistics Reference Online* (1st ed., pp. 1–11).  
 327 Wiley. <https://doi.org/10.1002/9781118445112.stat08290>
- 328 Gilchrist, R. M., Hall, R. A., Bacon, J. C., Rees, J. M., & Graham, J. A. (2020). Increased dispersion of oil from a  
 329 deep water seabed release by energetic mesoscale eddies. *Marine Pollution Bulletin*, 156, 111258.  
 330 <https://doi.org/10.1016/j.marpolbul.2020.111258>
- 331 Gladyshev, S., Talley, L., Kantakov, G., Khen, G., & Wakatsuchi, M. (2003). Distribution, formation, and seasonal  
 332 variability of Okhotsk Sea Mode Water. *Journal of Geophysical Research: Oceans*, 108(C6).  
 333 <https://doi.org/10.1029/2001JC000877>
- 334 Ji, J., Dong, C., Zhang, B., Liu, Y., Zou, B., King, G. P., Xu, G., & Chen, D. (2018). Oceanic Eddy Characteristics  
 335 and Generation Mechanisms in the Kuroshio Extension Region. *Journal of Geophysical Research: Oceans*,  
 336 123(11), 8548–8567. <https://doi.org/10.1029/2018JC014196>
- 337 Jing, Z., Chang, P., Shan, X., Wang, S., Wu, L., & Kurian, J. (2019). Mesoscale SST Dynamics in the Kuroshio–  
 338 Oyashio Extension Region. *Journal of Physical Oceanography*, 49(5), 1339–1352.  
 339 <https://doi.org/10.1175/JPO-D-18-0159.1>
- 340 Jing, Z., Wang, S., Wu, L., Chang, P., Zhang, Q., Sun, B., Ma, X., Qiu, B., Small, J., Jin, F.-F., Chen, Z., Gan, B.,  
 341 Yang, Y., Yang, H., & Wan, X. (2020). Maintenance of mid-latitude oceanic fronts by mesoscale eddies.  
 342 *Science Advances*, 6(31), eaba7880. <https://doi.org/10.1126/sciadv.aba7880>
- 343 Laxenaire, R., Speich, S., Blanke, B., Chaigneau, A., Pegliasco, C., & Stegner, A. (2018). Anticyclonic Eddies  
 344 Connecting the Western Boundaries of Indian and Atlantic Oceans. *Journal of Geophysical Research: Oceans*,  
 345 123(11), 7651–7677. <https://doi.org/10.1029/2018JC014270>
- 346 Laxenaire, R., Speich, S., & Stegner, A. (2019). Evolution of the Thermohaline Structure of One Agulhas Ring  
 347 Reconstructed from Satellite Altimetry and Argo Floats. *Journal of Geophysical Research: Oceans*, 124(12),  
 348 8969–9003. <https://doi.org/10.1029/2018JC014426>

- Laxenaire, R., Speich, S., & Stegner, A. (2020). Agulhas Ring Heat Content and Transport in the South Atlantic Estimated by Combining Satellite Altimetry and Argo Profiling Floats Data. *Journal of Geophysical Research: Oceans*, 125(9). <https://doi.org/10.1029/2019JC015511>
- Masuzawa, J. (1969). Subtropical mode water. *Deep Sea Research and Oceanographic Abstracts*, 16(5), 463–472. [https://doi.org/10.1016/0011-7471\(69\)90034-5](https://doi.org/10.1016/0011-7471(69)90034-5)
- McGillicuddy, D. J., Anderson, L. A., Bates, N. R., Bibby, T., Buesseler, K. O., Carlson, C. A., Davis, C. S., Ewart, C., Falkowski, P. G., Goldthwait, S. A., Hansell, D. A., Jenkins, W. J., Johnson, R., Kosnyrev, V. K., Ledwell, J. R., Li, Q. P., Siegel, D. A., & Steinberg, D. K. (2007). Eddy/Wind Interactions Stimulate Extraordinary Mid-Ocean Plankton Blooms. *Science*, 316(5827), 1021–1026. <https://doi.org/10.1126/science.1136256>
- McGillicuddy, D. J., Robinson, A. R., Siegel, D. A., Jannasch, H. W., Johnson, R., Dickey, T. D., McNeil, J., Michaels, A. F., & Knap, A. H. (1998). Influence of mesoscale eddies on new production in the Sargasso Sea. *Nature*, 394(6690), 263–266. <https://doi.org/10.1038/28367>
- Nakano, H., Tsujino, H., Sakamoto, K., Urakawa, S., Toyoda, T., & Yamanaka, G. (2018). Identification of the fronts from the Kuroshio Extension to the Subarctic Current using absolute dynamic topographies in satellite altimetry products. *Journal of Oceanography*, 74(4), 393–420. <https://doi.org/10.1007/s10872-018-0470-4>
- Oka, E., Kouketsu, S., Toyama, K., Uehara, K., Kobayashi, T., Hosoda, S., & Suga, T. (2011). Formation and Subduction of Central Mode Water Based on Profiling Float Data, 2003–08. *Journal of Physical Oceanography*, 41(1), 113–129. <https://doi.org/10.1175/2010JPO4419.1>
- Pegliasco, C., Chaigneau, A., & Morrow, R. (2015). Main eddy vertical structures observed in the four major Eastern Boundary Upwelling Systems. *Journal of Geophysical Research: Oceans*, 120(9), 6008–6033. <https://doi.org/10.1002/2015JC010950>
- Pujol, M.-I. (2022). *PRODUCT USER MANUAL For Sea Level Altimeter products* [dataset]. Copernicus Marine Service. <https://doi.org/10.48670/moi-00148>
- Qiu, B., & Chen, S. (2010). Eddy-mean flow interaction in the decadal modulating Kuroshio Extension system. *Deep Sea Research Part II: Topical Studies in Oceanography*, 57(13–14), 1098–1110. <https://doi.org/10.1016/j.dsr2.2008.11.036>
- Saito, H., Suga, T., Hanawa, K., & Watanabe, T. (2007). New type of pycnostad in the western subtropical-subarctic transition region of the North Pacific: Transition Region Mode Water. *Journal of Oceanography*, 63(4), 589–600. <https://doi.org/10.1007/s10872-007-0052-3>
- Sambe, F., & Suga, T. (2022). Unsupervised Clustering of Argo Temperature and Salinity Profiles in the Mid-Latitude Northwest Pacific Ocean and Revealed Influence of the Kuroshio Extension Variability on the Vertical Structure Distribution. *Journal of Geophysical Research: Oceans*, 127(3), e2021JC018138. <https://doi.org/10.1029/2021JC018138>
- Sun, W., Dong, C., Wang, R., Liu, Y., & Yu, K. (2017). Vertical structure anomalies of oceanic eddies in the Kuroshio Extension region. *Journal of Geophysical Research: Oceans*, 122(2), 1476–1496. <https://doi.org/10.1002/2016JC012226>
- Sun, Y., & Genton, M. G. (2011). Functional Boxplots. *Journal of Computational and Graphical Statistics*, 20(2), 316–334. <https://doi.org/10.1198/jcgs.2011.09224>
- Usui, N., Wakamatsu, T., Tanaka, Y., Hirose, N., Toyoda, T., Nishikawa, S., Fujii, Y., Takatsuki, Y., Igarashi, H., Nishikawa, H., Ishikawa, Y., Kuragano, T., & Kamachi, M. (2017). Four-dimensional variational ocean reanalysis: A 30-year high-resolution dataset in the western North Pacific (FORA-WNP30). *Journal of Oceanography*, 73(2), 205–233. <https://doi.org/10.1007/s10872-016-0398-5>
- Ward, J. H. (1963). Hierarchical Grouping to Optimize an Objective Function. *Journal of the American Statistical Association*, 58(301), 236–244. <https://doi.org/10.1080/01621459.1963.10500845>
- Yang, H., Qiu, B., Chang, P., Wu, L., Wang, S., Chen, Z., & Yang, Y. (2018). Decadal Variability of Eddy Characteristics and Energetics in the Kuroshio Extension: Unstable Versus Stable States. *Journal of Geophysical Research: Oceans*, 123(9), 6653–6669. <https://doi.org/10.1029/2018JC014081>
- Yasuda, I. (1997). The origin of the North Pacific Intermediate Water. *Journal of Geophysical Research: Oceans*, 102(C1), 893–909. <https://doi.org/10.1029/96JC02938>
- Yu, X., Naveira Garabato, A. C., Martin, A. P., Buckingham, C. E., Brannigan, L., & Su, Z. (2019). An Annual Cycle of Submesoscale Vertical Flow and Restratification in the Upper Ocean. *Journal of Physical Oceanography*, 49(6), 1439–1461. <https://doi.org/10.1175/JPO-D-18-0253.1>